Fuel 271 (2020) 117495

Contents lists available at ScienceDirect

Fuel

journal homepage: www.elsevier.com/locate/fuel

Full Length Article

Computational fluid dynamic simulations of thermochemical conversion of pulverized biomass in a dilute flow using spheroidal approximation

Ning Guo[a], Ángel David García Llamas[b], Tian Li[a,*], Kentaro Umeki[b], Rikard Gebart[b], Terese Løvås[a]

[a] Department of Energy and Process Engineering, Faculty of Engineering, NTNU – Norwegian University of Science and Technology, Trondheim, Norway
[b] Energy Engineering, Division of Energy Science, Luleå University of Technology, Luleå, Sweden

ARTICLE INFO

Keywords:
Spheroidal particle
Pulverized biomass
CFD
Entrained flow gasifier
OpenFOAM

ABSTRACT

A drag force model for spheroids, referred as the spheroid model, was implemented in OpenFOAM, in order to better predict the thermochemical conversion of pulverized biomass. Our previous work has found that the spheroid model predicts more dispersed results in terms of particle velocities and local concentrations comparing to other conventional particle models under non-reactive conditions. This work takes the spheroid model one step further, by validating against experiments performed under *reactive* conditions with a newly implemented heat transfer model for spheroids as well as updated devolatilization kinetic parameters. In addition, simulations were conducted in a configuration similar to a pilot-scale entrained flow gasifier for more realistic scenarios. Particle mass and axial velocity development were compared accordingly using four different modelling approaches with increasing complexity. When compared with models of spheroidal shape assumptions, the sphere and simplified non-sphere model predict 61% and 43% longer residence times, respectively. The combination of the spheroid shape assumption with the heat transfer model for spheroids tends to promote drying and devolatilization. On the other hand, the traditional spherical approach leads to longer particle residence times. These opposing effects are believed to be a major contributing factor to the fact that no significant differences among modelling approaches were found in terms of syngas production at the outlet. Furthermore, particle orientation information was reported in both experiments and simulations under reactive conditions. Its dependency on gas velocity gradient under reactive conditions is similar to what was reported under non-reactive conditions.

1. Introduction

The transport sector is a major emitter of harmful pollutants and accounted for approximate 25% of the global CO_2 emissions in 2016 according to International Energy Agency [1]. As an alternative to traditional liquid fossil fuels, biofuels present a great potential in reducing carbon emissions in this sector [2]. One viable option of producing biofuels is to use gasification technology to gasify pre-treated pulverized biomass to produce syngas; the produced syngas can then be converted to biofuels through Fischer-Tropsch synthesis [3]. Entrained flow gasification is believed to be a promising option for gasification technology, since it is highly efficient, produces less tar in the flue gas and can be employed on large scales [4]. As part of optimizing the underlying thermal conversion of the solid biomass, it becomes necessary to understand the details of the physical and chemical processes involved, both through experimental investigation as well as modelling and simulation. This involves comprehensive studies of gas-particle flows under reacting, and sometime highly turbulent, conditions.

The shape of the pulverized biomass has been given considerable attention in recent works. Results from several research groups have repeatedly shown that pulverized biomass particles are irregularly shaped due to their fibrous structure [5–7]. However, it is common practice for simplicity to assume that pulverized biomass particles are spherical [8–10]. This approach could potentially lead to simulation results significantly deviating from reality as particle shape is known to affect particle behaviors in terms of hydrodynamics and hence thermochemical conversion. Modelling and experimental efforts investigating the shape effects have been made for both coal particles [11–13] and biomass particles [14,15]. However, studies of biomass in a condition that is similar to entrained flow gasification are scarce.

To address this issue, a reasonable first step is to study non-spherical particle hydrodynamic behaviors under non-reactive conditions. Trubetskaya et al. [16] provided an approach that uses an infinite cylinder with volume-to-surface ratio (based on 2D dynamic imaging

* Corresponding author.
E-mail address: tian.li@ntnu.no (T. Li).

https://doi.org/10.1016/j.fuel.2020.117495
Received 18 November 2019; Received in revised form 3 February 2020; Accepted 27 February 2020

Nomenclature

A	Pre-exponetional factor [s^{-1}]
d_{eq}	Equivalent diameter [m]
D	Diameter of inner central tube in Section 4 [mm]
E	Activation Energy [J·kmol^{-1}]
KG	The Kishore-Gu model
m	Mass [kg]
m_{devol}	Remaining volatile in the particle [kg]
Nu	Nusselt number
Pr	Prandtl number
R	Universal gas constant [J·k^{-1}·kmol^{-1}]
RM	The Ranz-Marshall model
r	Radial position [m]
Re	Reynolds number
T_p	Particle temperature [K]
x, y, z	x, y, z (or axial) position [m]
λ	Particle aspect ratio
0	Initial stage

measurement) to represent the various distribution of sizes and shapes of biomass particles in combustion models. Haider and Levenspiel [17], Zastawny et al. [18], Rosendahl [19], and Hölzer and Sommerfield [20] proposed various drag force models for particles of various shapes, such as cylinders, elliposoids, discs, fibers and other non-spherical particles. Jeffery [21] and Rosendahl [19] reported on different models for particle torques depending on particle shape. Based on their work, our previous study considered pulverized biomass particles to be prolate spheroids and investigated the effects on particle velocity, residence time and local concentration under non-reactive conditions, quantitatively with considerations of particle torques [22]. It was found that different shape assumptions lead to different predictions of particle residence times and local concentrations [22].

Given the aforementioned findings under non-reactive conditions, one can postulate that the particle shape plays an important and complex role also under reactive conditions. Non-spherical particles have larger ratios of surface area to volume than spherical particles. Additionally, morphological changes occur during the particle thermochemical conversion as evidenced by Panahi et al. [7], which are difficult to predict. They influence particle heat and mass transfer, hence affecting drying, devolatilization and char conversion. Lu et al. [15] investigated effects of particle shapes on biomass devolatilization, and both experiments and simulations show that less symmetrical particles react faster than near spherical particles, which indicates that shape irregularity impacts the overall conversion rate already at relatively small particle sizes (~320 μm). This is confirmed by the analytical study of Li and Zhang [23] who found that the aspect ratio of particles presents a positive correlation to char combustion rate under forced convection.

All of the works mentioned above point towards the importance of accurately modelling the force, torque, shape and surface area of particles as non-spherical under reactive conditions. Various attempts have been made to address these problems in reactive multi-particle settings [24]. One approach is to introduce a shape factor to account for particle shape irregularities, such as the work of Bhuiyan and Naser [25], who modelled co-firing process of biomass and coal under oxy-fuel conditions. Another alternative approach is to employ a more sophisticated particle hydrodynamics model with considering particle orientations and directionalities. Bonefacic et al. [26] and Yin et al. [27] both conducted numerical studies for co-firing biomass with coal and compared differences between two modelling methods (spherical and cylindrical shape assumptions for biomass particles). Bonefacic et al. [26] found that the concentrations of carbon monoxide and nitrogen monoxide in the flue gases were more accurately predicted when using the cylindrical shape assumption than the spherical one, even though biomass only makes up 20% weight in the biomass/coal fuel mixture. Yin et al. [27] found that biomass volatiles were released earlier and more completely in simulation with cylindrically shaped biomass particles when compared to spherical ones. Even though some of these studies compared simulation results with experimental data of gas species, their simulations were not compared with experimental data of the particles themselves. In addition, to the authors' best knowledge, a thorough comparison of these different modelling approaches under entrained flow gasification of only pulverized biomass has not been conducted and their effects on the resulting syngas quality need to be examined.

Built on our previous non-reactive study [22], this work takes one-step further to study shape effects under reactive conditions and serves three purposes. First, it aims to quantitatively study the differences between the sphere model, the simplified non-sphere model and the spheroid model under reactive conditions. Subsequently, it provides information on particle orientation, which is usually not included in other simulation works. Thirdly, the results from simulations are compared with experimental results in terms of biomass particle hydrodynamics in a drop tube burner, which is rarely found in literature. The current work furthermore adapts the particle surface area to the prolate spheroid for more accurately capture the mass and heat transfer. A heat transfer model for spheroids and a new set of kinetic parameters for devolatilization that are more suitable for entrained flow gasification conditions are employed to better simulate thermochemical conversion of pulverized biomass. It should be noted that the main purpose of this paper is to study the shape effects of biomass particles in entrained flow gasification process using CFD simulations. It does not aim to assess different kinetic models for thermochemical biomass conversions, so only simple models are used in this regard.

The paper is divided in four sections. Section 2 outlines the theory and methodology of the three particle hydrodynamic models, heat transfer models and the devolatilization kinetic parameters. Section 3 compares simulations using the spheroid model to experiments in a lab-scale drop tube reactor under reactive conditions. Section 4 applies different particle shape and heat transfer approaches to an entrained flow gasifier for a comparative analysis and Section 5 summarizes the conclusions and gives future recommendations.

2. Modelling theory and methodology

The CFD simulations were conducted in an Eulerian-Lagrangian framework using the open source platform, OpenFOAM 4.1 and were solved with a modified solver based on coalChemistryFoam [28]. There are two options for modelling particle mass loss in OpenFOAM. The first one assumes that the particle size decreases, but its density remains constant. The other one assumes that the particle density decreases, but its size remains constant. Indeed, neither of them can reflect reality that both size and density changes attribute to the particle mass loss [29]. Additionally, the shrinkage behavior is still not well understood for sub-millimeter pulverized biomass particles under the investigated high temperature conditions. Due to the lack of overwhelming evidence of either models' superiority, the first option was chosen based on the work of Ku et al. [30]. This configuration in OpenFOAM would furthermore make it easier to implement changes to the particle aspect ratios in the future.

The theory and methodology is consistent with the work of Ku et al. [28] and will not be repeated here (the considered chemical reactions and their rates can be found in the Supplementary material). However, since this work investigates biomass particles using different shape approaches, only the different particle hydrodynamic models (Section

2.1) and heat transfer models (Section 2.2) are described in here in more detail, as to the work of Ku et al. [28] where the common practice of simulating pulverized biomass particles as spheres is employed. In addition, a new set of kinetic parameters for devolatilization is applied and is explained in Section 2.3.

2.1. Particle hydrodynamics

This section briefly explains the employed theory of particle hydrodynamics, as detailed information on particle hydrodynamics and underlying conservation equations can be found in our previous paper, i.e. Guo et al. [22]. In this work, all particles are subject to gravity and buoyancy in the simulations. In addition, three different particle models are used to account for particle drag and torque: the sphere model, the simplified non-sphere model and the spheroid model. The sphere model is a widely used approach and considers particles as spheres of equivalent volume [28]. As a result, all particles behave the same. The simplified non-sphere model, reported by Haider and Levenspiel [17], compensates for the effects of different particle shapes by introducing an overall shape factor to characterize particle shape irregularities. It represents a more realistic treatment of biomass particles, but still does not account for rotational motions of particles. The spheroid model treats particles as prolate spheroids. Particle drag force and torque are both calculated based on the work of Hölzer and Sommerfield [20] and Jeffery [21], respectively. The directions or orientations of the particles are considered by introducing overall, lengthwise and crosswise sphericity of the particle. When the spheroid model is applied, the particle surface area for heat and mass transport is corrected to the surface area of a spheroid. In addition, the current model allows for different particles having different aspect ratios, although it does not allow particle aspect ratio to change for the given particle throughout the thermochemical conversion process. It should be noted that several experiments have shown that biomass particles will indeed gradually transform into spherical geometries [7,31]. However, to the best knowledge of the authors, no good model has yet been proposed to account for a changing particle aspect ratio due to conversion, which is beyond the scope of the present work. The current spheroid model is for simplicity a point-based model with torque being one-way coupled and has potentials for further improvement. Ideally, to model the particle rotation, one should resolve the flow around the particles, which is computationally expensive. Even so, this still does not consider the morphological changes caused by the conversion processes. Additional forces may be introduced by those processes thus alternating particle orientations. However, these details are beyond the scopes of this work, which intends to provide a first-step simple tool to study the effect of particle shape and orientation, and to reveal the capacity of the implemented model, including the deficiencies.

2.2. Particle heat transfer model

It is common practice to model particle heat transfer by the Ranz-Marshall model for external convection [32,33]. In this model, the particle Nusselt number is calculated as:

$$Nu = 2 + 0.6Re^{\frac{1}{2}}Pr^{\frac{1}{3}} \tag{1}$$

where Nu is the particle Nusselt number, Re is Reynolds number and Pr is the Prandtl number. However, the Ranz-Marshall model is developed based on a spherical approach and employing it to simulate non-sphere particles could potentially lead to inaccurate predictions.

To remedy this, Kishore and Gu [34] proposed a simple Nusselt number correlation for spheroids:

$$Nu = 2\lambda^{0.3} + Pr^{0.4}\left(0.4Re^{0.5}\lambda^{0.83} + 0.06Re^{\frac{2}{3}}\lambda^{0.1}\right) \tag{2}$$

where λ is aspect ratio of the spheroid, here defined as the ratio of the particle's major to minor axis. It should be noted that the above correlation is limited to the following range of flow conditions: $1 \le Re \le 200$, $0.25 \le \lambda \le 2.5$ and $1 \le Pr \le 1000$. The applicability range of this model is somewhat different than that found typically in entrained flow gasifiers of pulverized biomass particles under atmospheric pressures. Particle Reynolds number of pulverized coal is reported to be mostly in the range of 1 and 10, but can reach up to 100 [35]. Since biomass particles tend to have larger sizes, their particle Reynolds numbers are subject to increase, depending on their pretreatment methods. The particle aspect ratio could also be smaller than 0.25 or larger than 2.5, depending on pretreatment process and morphological changes under reactive conditions, whereas the maximum particle aspect ratio used in this work is 10. In addition, the Prandtl number of the gas flow is estimated to be around 0.69–0.75 (based on Prandtl number of air at 0–1600 °C, 1 bar). Even though the particle flow in this work may be outside of the given applicability range, this correlation is applied here due to lack of other alternatives. This model is hereafter referred to as Kishore-Gu model.

2.3. Particle devolatilization

In entrained flow gasifiers, biomass particles are subject to fast heating rates, high peak temperatures and short residence times. To accommodate such conditions, the devolatilization kinetic parameters developed by Johansen et al. [31] is applied here. The devolatilization rate is formulated as a single-step first-order Arrhenius reaction as follows:

$$\frac{dm_{devol}}{dt} = -Ae^{-\frac{E}{RT_P}}m_{devol} \tag{3}$$

where m_{devol} is the remaining volatile in the particle [kg], t is time [s], A is pre-exponential factor (18.9×10^3 s^{-1}), E is the activation energy (2.1305×10^7 J·kmol^{-1}), R is the universal gas constant [J·K^{-1}·kmol^{-1}], and T_p is the particle temperature [K].

3. Comparison with experiment of a lab-scale reactor

The spheroid model has been previously validated under non-reactive conditions [22], and is in this paper further validated under reactive conditions. The simulations presented in this section are based on experiments of pulverized biomass particles injected through a laminar, flat flame assisted drop tube reactor. The experimental and simulation setups are described in Section 3.1, followed by a discussion of the resulting particle and flow axial velocities and particle alignment angles in Section 3.2.

3.1. Experiment and simulation setups

Fig. 1 presents a real photograph and 3D illustration of the flat flame drop tube reactor, which consists of biomass and gas feeder tubes, a porous flat flame burner, four windows for optical access, a reactor body, and exhaust tubes. The simulation geometry was simplified to consist of two cylindrical parts: feeder and reactor, as shown in Fig. 2. The feeder is a 100 mm long cylinder with a radius of 3.5 mm. The reactor is a 360 mm long cylinder with a radius of 40 mm. There are three inlets to the domain. *Inlet F* is a circular face with a diameter of 7 mm and acts as fuel inlet. *Inlet A* is an annular ring with 62.5 mm inner diameter and 73.5 mm outer diameter. *Inlet B* is an annular ring with 7 mm inner diameter and 62.5 mm outer diameter, and it represents the outlet of the porous flat flame burner in the experiment. The outlet is a circular face with a diameter of 71 mm. Other parts are treated as walls.

Selected gases with or without biomass particles were injected via these three inlets according to the experiment, as listed in Table 1. The protective N_2 was injected via *Inlet A*. Biomass particles were carried by CO_2 and injected through *Inlet F*. In the experiment, a mixture of CH_4, O_2 and CO_2 was supplied to the flat flame burner (i.e. prior to the

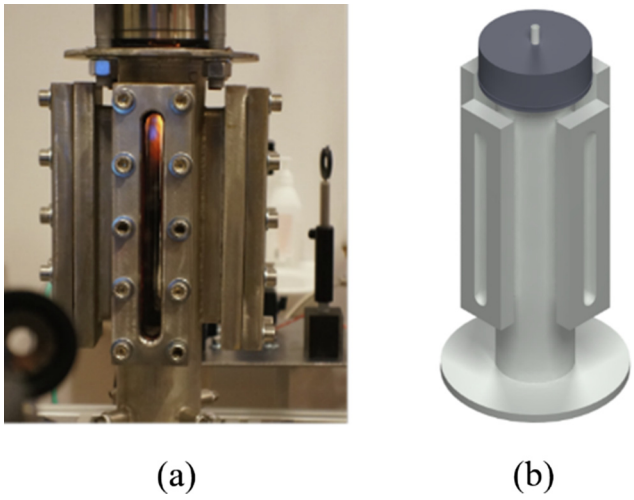

Fig. 1. Lab-scale flat flame drop tube reactor (a) photo; (b) simplified 3D illustration.

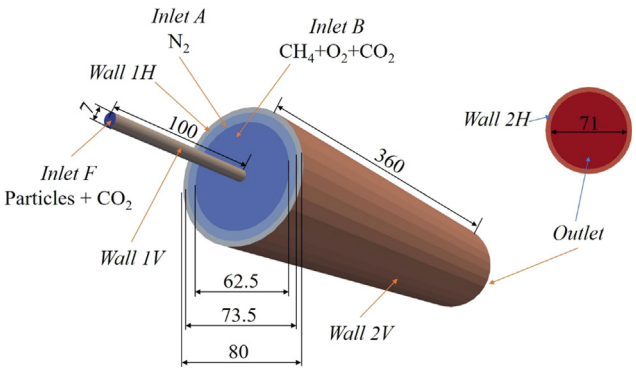

Fig. 2. Simulation geometry of the flat flame drop tube reactor. Dimension unit: mm.

laminar flame) and their flow rates are listed under *Inlet B* (experiment) in Table 1. The mixture was ignited and exited the burner (i.e. post-flame) via *Inlet B*. However, in order to save computational costs in the simulations, it is common not to include the combustion process of these gas mixtures in the burner. Chemical reactions are assumed to reach adiabatic equilibrium instead and the products (and their mass fractions) can therefore be calculated accordingly and used in the simulations [36,37]. Following this practice, the gas compositions listed under *Inlet B* (simulation, post-flame) in Table 1 were used as inlet boundary conditions in the simulations. The boundary conditions of the velocity for all these inlets were set to be uniform and were calculated based on their respective flow rates.

The temperature boundary conditions were configured as follows. It was assumed that the temperature of *Inlet F* was at room temperature (300 K). The same temperature was set for *Wall 1 V*, as the feeding tube was water cooled. As previously mentioned, *Inlet B* is where the outlet of the porous flat flame burner is located, and it was assumed that chemical equilibrium was achieved here. As a result, the adiabatic flame temperature upon chemical equilibrium, 2560 K, was used here. It should be mentioned that particles were expected to be dried fast at such high temperatures, so particle moisture was assumed to be 0% in Table 2. Based on experimental measurements, the temperature was assumed to be linearly dependent on the height. Therefore, *Inlet A* and *Wall 1H* were set to be 838 K, *Outlet* and *Wall 2H* were set to be 583 K, and *Wall 2 V* had a temperature profile linearly interpolated between these two values.

Table 2
Particle composition in the simulations of drop-tube reactor. Volatile gases and their percentages are based on the beech wood data from Ku et al. [28].

Component	Mass fraction
Volatile	81.16%
CH_4	14.77%
H_2	2.39%
CO_2	33.57%
CO	30.42%
Moisture	0% (dried wood)
Fixed carbon	18.42%
Ash	0.42%

The biomass particles used in the experiments were Norwegian spruce (picea abies). Hence the initial particle density was assumed to be 1100 kg/m^3 with zero porosity, based on the previous work of Li et al. [5]. Similar skeletal densities in the range of 900–1200 kg/m^3 have also been reported in other simulation works [36,38]. For simplicity it is assumed that there is no porosity within the biomass particles in the current CFD simulations. The particle sizes were configured according to the experiment, represented by a Rosin-Rammler distribution as shown in Fig. 3. The relationship between the particles' equivalent diameter and aspect ratio was measured in the experiment as shown in Fig. 4, and a simple polynomial formula was used to reflect this trend in the simulations. The particle composition used in the simulation is listed in Table 2, where volatile gases and their percentages are based on the beech wood data from Ku et al. [28]. Most of the particles were expected to be in the drying and devolatilization stages. Released volatiles were modelled based on the same devolatilization model and kinetic parameters, regardless of species. Given that the ratio of particle to gas flow mass (or volume) fraction was so low here, the chemical effects of composition of volatile species were expected to be insignificant. Therefore, the estimation of the volatile species and their percentages used in Table 2 is considered sufficiently appropriate in this context. In terms of particle initial orientation, due to the lack of experimental data on this particular point, it was assumed that every one third of particles have their major axes parallel to the *x*-, *y*- and *z*-directions respectively in the gas flow frame when the spheroid model is used. After conducting grid independence tests based on axial velocities of gas flow under reactive conditions without injecting biomass particles, a mesh of 184,960 hexahedral cells was used for further simulations in this section, together with the spheroid model and the Kishore-Gu model.

Table 1
Gases injected via different inlets. The unit "slpm" means standard liter per minute.

Location	Parameter	Unit	N_2	CO_2	CH_4	H_2	O_2	CO	H_2O
Inlet A	Volume flow rate	slpm	6.79	–	–	–	–	–	–
Inlet B (experiment)	Volume flow rate	slpm	–	3.58	4.29	–	5.36	–	–
Inlet B (simulation, post-flame)	Mass fraction	%	–	33.9	–	0.8	0.1	33.9	31.3
Inlet F	Volume flow rate	slpm	–	0.272	–	–	–	–	–

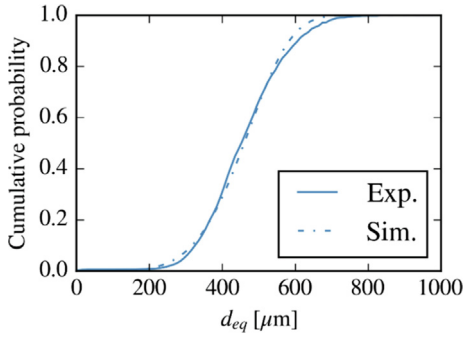

Fig. 3. Particle size distribution. "Exp." and "Sim." represent experiment and simulation data, respectively. d_{ep} is particle equivalent diameter.

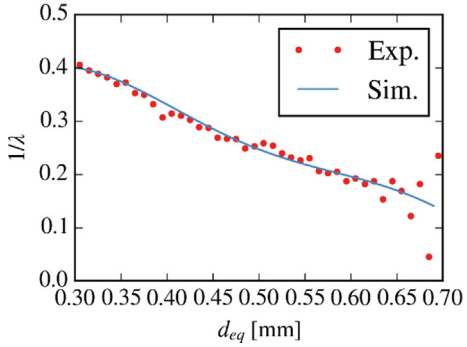

Fig. 4. The relationship between particle aspect ratio, λ, and equivalent diameter, d_{eq}. Only particles with equivalent diameter of 0.3–0.7 mm are shown in this figure as they make up around 90% of all the particles. "Exp." and "Sim." represent experiment and simulation data, respectively.

3.2. Results and discussions

3.2.1. Gas flow axial velocities under non-reactive conditions

Fig. 5 presents the axial velocities of the gas flow at different positions away from the burner outlet under non-reactive conditions, without injecting any biomass particles. It provides an overview of the overall gas flow fields, without the complications and influences of chemical reactions and biomass particles. One can see that there is less or even no experimental data outside the radial position of ± 3.5 mm. This is because the experimental data for gas flow was obtained based on tracer particles (TiO_2) injected via *Inlet F*, located within the radial position of ± 3.5 mm. From upstream to downstream (i.e. from 0 mm to 70 mm away from burner outlet), the stream wise axial velocity of the gas flow increase, both in the experiments and the simulations. Since the gas at *Inlet F* (radial position within ± 3.5 mm) had a lower volumetric flow rate per cross-sectional area than that of *Inlet B* (radial position between ± 3.5 mm and ± 31.25 mm, part of which is outside the radial range shown in Fig. 5), the aforementioned increasing trend in axial velocity is expected, as the gas from *Inlet F* was accelerated by the gas from *Inlet B*. The simulation match reasonably with the experiment, especially in the middle region of the radial position and from 20 mm to 50 mm away from burner outlet. However, further up-stream some deviation is noted. Several reasons can contribute to this discrepancy. First, asymmetries in the experiment can be clearly detected. This might be caused by the biomass feeder not being completely perpendicular to the ground level in the experimental setup. Furthermore, the experimental data in the upstream (0 mm and 11 mm away from burner outlet) may also be less reliable, due to the fact that the tracer particles had just left the burner outlet and entered the measuring laser plane. In theory, a tracer particle needs to be optically measured twice for post-processing to calculate its velocity based on its time and position at the two measuring points. There is a possibility that some particles that just entered or left the laser plane were only optically measured once, which makes their velocity calculations by the post-processing routine less reliable. Given these factors, it is possible to conclude that the simulations and experiments match reasonably well, apart from close to the inlet, which forms the basis for further simulations with reactive biomass particles.

3.2.2. Particle axial velocities under reactive conditions

Fig. 6 shows axial velocities of biomass particles, along the radial direction of the reactor, at different positions downstream from the burner outlet under *reactive* conditions. By comparison, good agreements between simulation results and the experiments are achieved. Some discrepancies are evident and believed to be due to the same reasons as explained in 3.2.1, i.e. reactor asymmetry and particle measurement errors in and out of the laser plane. In the range from 0 mm to 70 mm downstream of the burner outlet, the experimental data indicates that the biomass particles first accelerate, then decelerate. This is not surprising, as when particles are transported further away from the burner outlet, the slip velocities become higher. As a result, drag forces acting on the biomass particles plays an increasing important role and eventually slows down the biomass particles. However, this observed deceleration could not be reproduced in the simulations downstream of the burner outlet. One possible cause could be temperature differences between the experiments and the simulation. The temperature boundary conditions in the simulation were configured only based on a few measurement points at the reactor wall, which may give rise to uncertainties related to temperature predictions in the downstream. This likely results in an over prediction of the gas temperature in the downstream, thus also an over prediction of the gas velocity, supported by the observation of higher particle velocities in the simulations. In addition, the contribution to mass losses based on particle size, aspect ratio and density affect the balance between drag and gravity. The biomass particles in the simulation were assumed to have constant density and aspect ratio. Their mass loses were reflected by size changes only, which is a known shortcoming of the models compared to the experiment. Also, Panahi et al. [7] observed particle spherodization phenomena when biomass particles went through pyrolysis at high temperatures, which was not included in the models in the current simulations. It was also observed that a certain number of biomass particles had sudden changes to their trajectories in the experiments. Similar phenomena was also reported by Elfasakhany et al. [39] and they argued this was caused by the rapid release of volatiles from fibrous biomass particles. This could also explain certain standard deviation exists in the experiments, while biomass particles in the simulation tend to have very similar axial velocities.

3.2.3. Particle projected alignment angles under reactive conditions

The particle alignment angle is here defined as the angle between the particle's major axis and the gravity direction. It is an important parameter for determining the particles' hydrodynamics, as particle force and toque are coupled in the present spheroid model. The probability density function of particle projected alignment angles at different positions away from burner outlet is presented in Fig. 7. Projected values are used instead of real 3D values as the current experimental setup can only generate one single laser plane for each measurement. Note that the term "projected" value is conceptually the same in the experiments and the simulations, but differ slightly in their respective post-processing methodologies. In the experiment, biomass particles, shone through by laser, have projections in the laser plane, and these projections are the basis to derive projected alignment angles. In the simulations, a virtual plane is created for each particle and it is defined by the gravity line and the particle point, and the particle projected alignment angle is calculated based on its projection on this virtual plane. In the upstream close to the burner outlet, the particle projected alignment angles are in the experiments distributed between 0 and 90° with a preferential concentration close to 0°. As the biomass

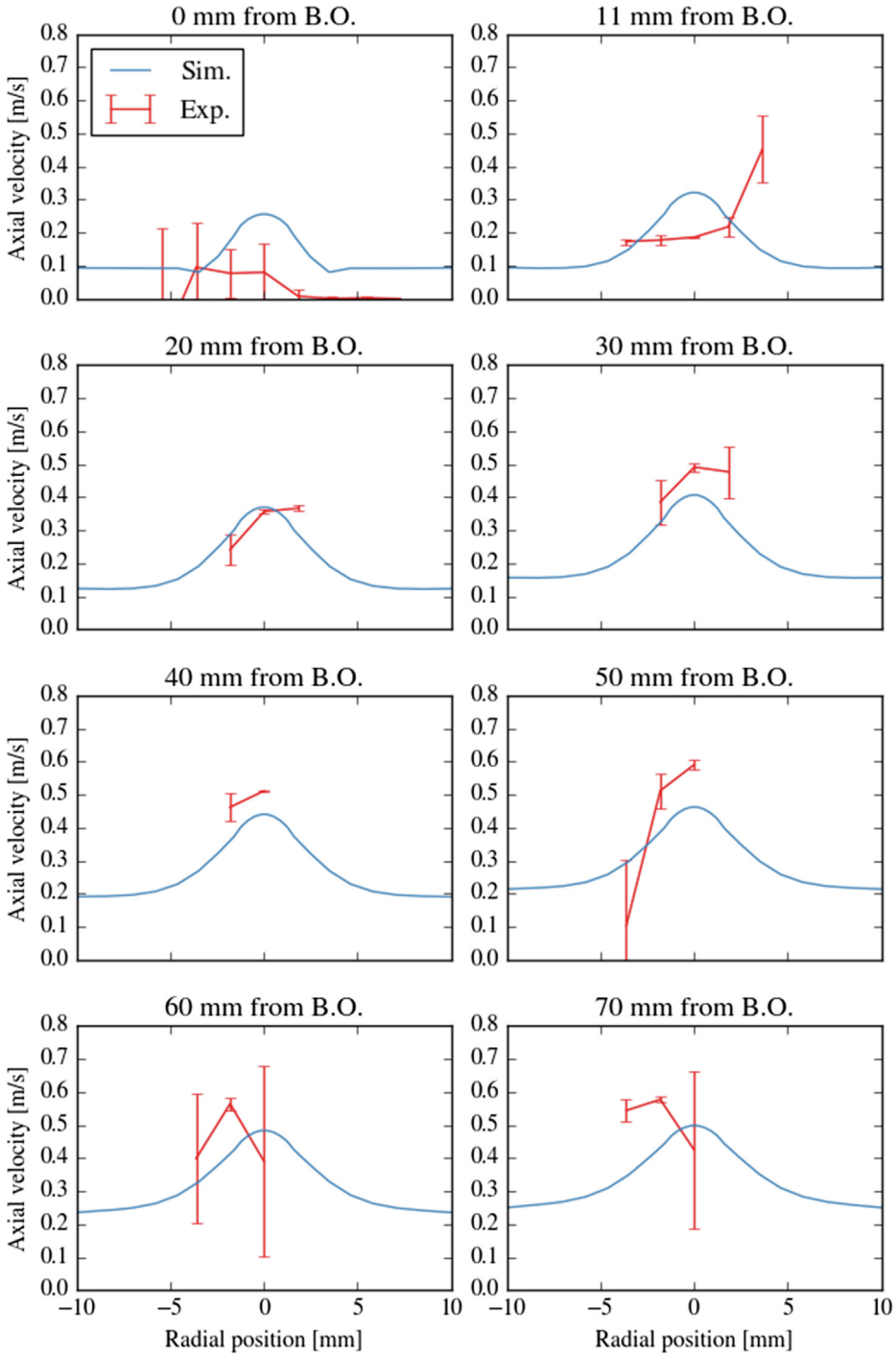

Fig. 5. Axial velocities of gas flow fields along the radial direction of reactor at different positions away from burner outlet under non-reactive conditions without injecting biomass particles. TiO_2, injected through *Inlet F*, acts as tracer particles to obtained velocity data in the experiment. "B.O." stands for burner outlet where Inlet *B* is located. "Sim." and "Exp." mean simulations and experiments, respectively, and are marked by blue and red solid lines, respectively. Error bars represent standard deviations. (For interpretation of the references to color in this figure legend, the reader is referred to the web version of this article.)

particles are transported further away from the burner outlet downstream, this preference towards 0° became even more evident. This trend, however, is not reflected in the simulations. At the outlet, numerical results show that one third of particles tend to have projected alignment angles of 0°, while the other two thirds have 90°. This is however in line with the initial configurations of particles upon injection, where every one third of particles have their major axes parallel to *x*-, *y*- and *z*-directions respectively. As particles are transported downstream, their projected alignment angles are more randomly distributed over the range between 0° and 90°. Njobuenwe and Fairweather [40] have shown that for inertial fibers in turbulent flows, the fiber is mostly anisotropically aligned with the flow direction, where large velocity gradient exists, otherwise they are isotropically aligned. Based on the axial velocity data under non-reactive conditions presented in Fig. 5, it is reasonable to assume that velocity gradients in the experiments were more evident than simulations due to thermal expansion of gas flow fields under reactive conditions.

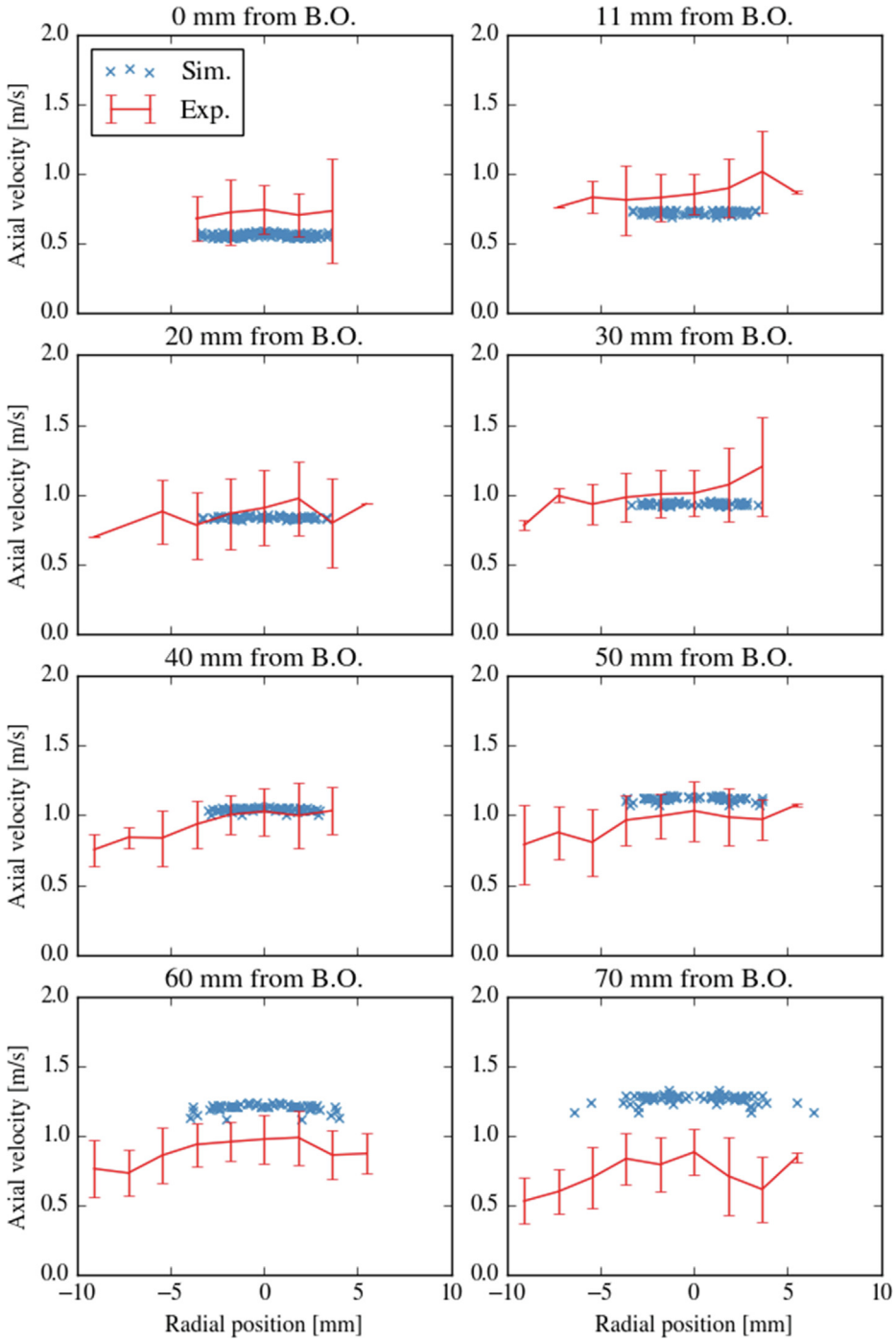

Fig. 6. Axial velocities of biomass particles along reactor radius at different positions away from burner outlet under reactive conditions. "B.O." stands for burner outlet. "Sim." and "Exp." mean simulations and experiments, respectively, and are marked by blue crosses and red solid lines, respectively. Error bars represent standard deviations. (For interpretation of the references to color in this figure legend, the reader is referred to the web version of this article.)

4. Application to a simplified entrained flow gasifier

In this section, the aforementioned three different particle models are applied to simulate entrained flow gasification of pulverized biomass under close to realistic operating conditions. A simplified simulation configuration is a setup based on a pilot-scale entrained flow gasifier as described in earlier sections and is outlined Section 4.1. In Section 4.2, results are presented based on the three particle models as presented above.

4.1. Simulation configurations

In Section 3, a laminar lab-scale reactor was simulated, and a reasonable next step is to scale up and apply the simulation models to a larger and turbulent reactor under more realistic operating conditions. Hence, the pilot-scale entrained flow gasifier reported by Simonsson et al. [41] was chosen as a comparative target for the simulations. As seen in Fig. 8, the gasifier was simplified into two parts, feeder and reactor. The feeder is 100 mm long and has two air registers, inner central tube and outer annular tube. Primary air was injected with biomass into the 50 mm diameter central tube. Secondary air entered

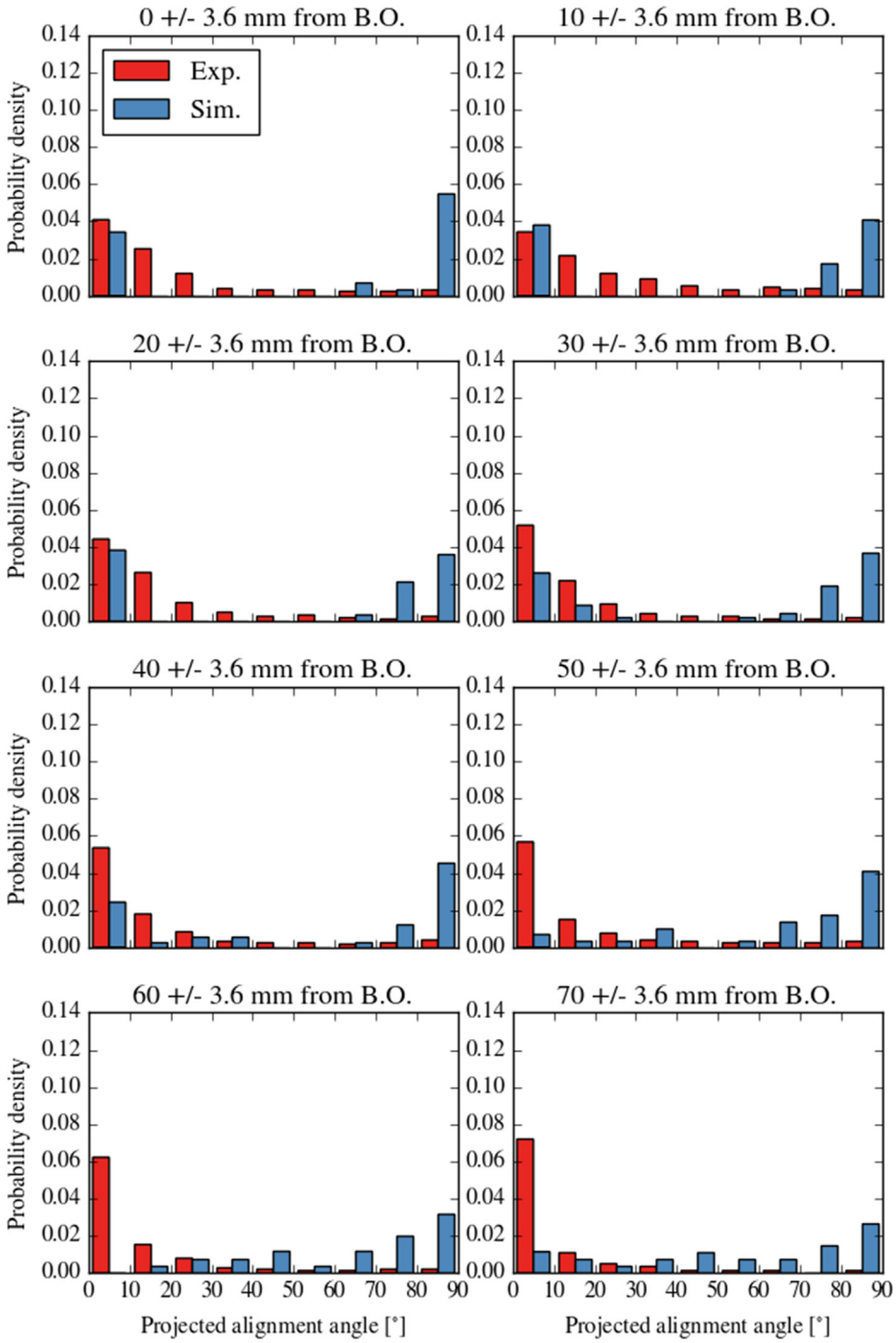

Fig. 7. Probability density of projected alignment angle of biomass particles at different positions away from burner outlet under reactive conditions. "B.O." stands for burner outlet. "Exp." and "Sim." mean experiments and simulations, respectively, and are marked by red and blue bars, respectively. (For interpretation of the references to color in this figure legend, the reader is referred to the web version of this article.)

via the annular tube with diameter of 52 mm and 56 mm. The reactor part is a 3.5 m long cylinder with diameter of 50 cm.

Boundary and initial conditions were configured based on the operating conditions with an 0.5 air-fuel equivalence ratio, as stated in Simonsson et al. [41]. Primary air was injected at 535 $l \cdot min^{-1}$, secondary air was injected at 410 $l \cdot min^{-1}$ with 3172 rpm to provide swirl. Inlet temperature was set at 300 K. The wall and the internal initial temperature were set at 1428.46 K, based on the experimental measurement by Simonsson et al. [41]. Standard k-ε model was employed to simulate the flows. A mesh of 1872910 hexahedral cells was selected for further simulations after a grid independence test based on centerline temperature results from reactive simulations without injecting biomass particles.

Pulverized biomass particles were injected at 20.2 $kg \cdot h^{-1}$. The particle composition is listed in Table 3. The volatile gases and their percentages are based on the data from Thunman et al. [42], which is summarized in Haseli et al. [43]. The original paper presenting the experiments (Simonsson et al. [41]) did not provide approximate analysis of the volatiles. However, the goal is to compare the differences between four particle modelling approaches in a realistic configuration. Therefore, the volatile data used here in the current CFD simulations could sufficiently serve the purpose. The particle density is 1100 kg/m^3

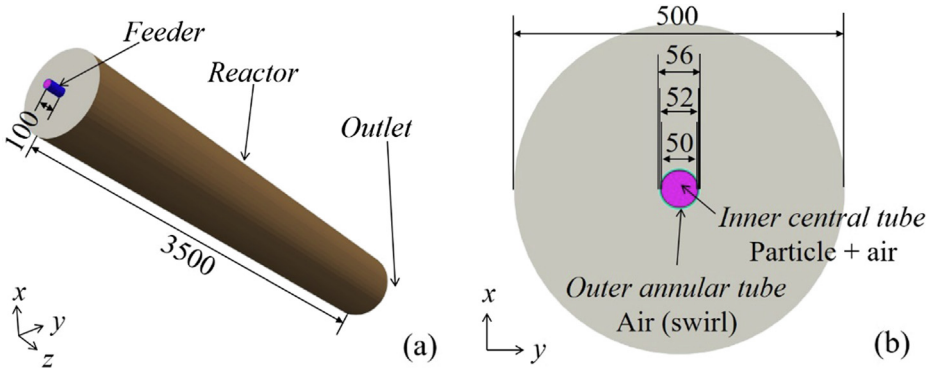

Fig. 8. Simulation geometry in (a) 3D and (b) *xy*-plane, based on experiments from Simonsson et al. [41]. Dimension unit: mm.

Table 3
Particle composition in the simulations of entrained flow gasifier. Volatile gases and their percentages are based on the data from Thunman et al. [42], which is summarized in Haseli et al. [43].

Component	Mass fraction
Volatile	76.90%
H_2	0.54%
CO	31.84%
CO_2	14.30%
H_2O	14.30%
CH_4	15.92%
Moisture	7.70%
Fixed carbon	15.10%
Ash	0.30%

as discussed in Section 3. The particle size distribution is described in Fig. 9. The particle aspect ratio is set to 10 based on our previous study [22], as this was not reported in the experimental work from Simonsson et al. [41]. There are two reasons that the aspect ratio is intentionally configured this way. First, Panahi et al. [7] has reported that the average aspect ratio could be 8.2 for beech wood particles whose average dimensions are 190 × 1500 μm. Second, the simulations are intended to highlight the differences among the different modelling approaches, rather than to compare with experimental results. Therefore, a slightly higher aspect ratio could make the differences among the four approaches more pronounced and serves the purpose of the simulations presented in this section.

Depending on the configurations of the biomass particle models, simulations of four cases are presented in this section, which are listed in Table 4. There are two major motivations to employ such case configurations. The first one is to study the effects of different particle hydrodynamic models based on different assumptions of particle shape. Hence the sphere model was used in *Case 1*, the simplified non-sphere model was used in *Case 2*, the spheroid model was used in *Case 3* and *4*, where particle initial orientations were configured as the same as in Section 3. The other reason is to investigate the impact of the choice of particle heat transfer model. It is common to only use a spherical based heat transfer model, which deviates from the fact that biomass particles are non-spherical. As a result, in *Case 3* and *4*, the Ranz-Marshall model and Kishore-Gu model were used, respectively, here also in combination with the spheroid particle model to study their differences in simulations of entrained flow gasification of pulverized biomass particles.

4.2. Results and discussions

Most results in this section are presented along reactor radial direction, r/D, at different heights, z/D, of the reactor. r is the radial position of the reactor, z is the axial position of the reactor and D is the diameter of the inner tube where biomass particles are injected. The inner central tube, where biomass and air were injected, is located at radial direction of r/D = 0–0.5. The outer annular tube, where secondary air with swirl was injected, is located at radial direction of r/D = 0.52–0.56. The reactor wall is located at radial direction of r/D = 5. The inner inlet is located at z/D = −0.2, and the outer annular inlet is located at z/D = 0, which is also the start of the reactor. The outlet of the reactor is located at axial position of z/D = 70. All the results below are sampled at 12 s after particle injections start. When particles are sampled at different heights of the reactor, a z/D tolerance of ± 0.05 is applied, which is consistent with our previous non-reactive study [22].

4.2.1. Particle conversion

The rate of particle conversion can be represented by the normalized biomass particle mass, m/m_0, which is defined as the remaining mass of a particle, m, over the initial mass of the same particle, m_0. Fig. 10 shows normalized particle mass along the reactor radial direction (r/D) at different heights (z/D) along the reactor, but only particles with short residence times are sampled. The sampling method is explained as follows. It is reasonably assumed that most of the biomass particles could travel faster than 2 $m{\cdot}s^{-1}$ in the axial direction without recirculation, based on the results later shown in Fig. 12. The residence time of a particle with axial velocity of 2 $m{\cdot}s^{-1}$ is used as threshold here. A biomass particle reaching the plotted axial position (z/D) is included if its residence time is shorter than or equal to the threshold, otherwise it is excluded. The reason for this sampling method is to exclude biomass particles that were trapped in recirculation zones of gas flow fields for a long time, so heat transfer can be studied with minimum influence of particle residence time. Of course, this sampling method is not perfect and, by its definition, will include or exclude particles that contradicts to the original sampling intention. However, it is a fast and simple method that can present an overview of biomass particles outside recirculation zones with tolerable errors. In addition, particles that have entered char conversion stages are excluded in

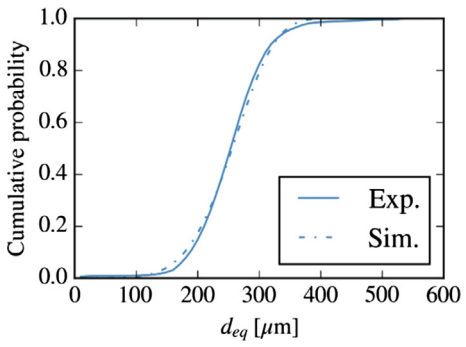

Fig. 9. Particle size distribution. "Exp." and "Sim." represent experiment and simulation data, respectively. d_{ep} is particle equivalent diameter.

Table 4
Particle model configurations in different simulation cases.

Case No.	Case name	Particle shape	Particle hydrodynamics	Particle heat transfer	Surface area in char surface reaction
1	sphere	Sphere	The sphere model	Ranz-Marshall	Sphere of equivalent volumes
2	nonSphere	Non-sphere	The simplified non-sphere model	Ranz-Marshall	Sphere of equivalent volumes
3	spheroidRM	Spheroid	The spheroid model	Ranz-Marshall	Spheroid of equivalent volumes
4	spheroidKG	Spheroid	The spheroid model	Kishore-Gu	Spheroid of equivalent volumes

Fig. 10 since the difference is negligible and the focus here is on particles in drying and devolatilization stages.

The general trend is similar of all four cases, as shown Fig. 10. In the upstream where z/D is 0, the normalized particle mass of all cases is close to 1, as thermochemical conversion of biomass particles had just started or was about to start. As z/D increases, biomass particles

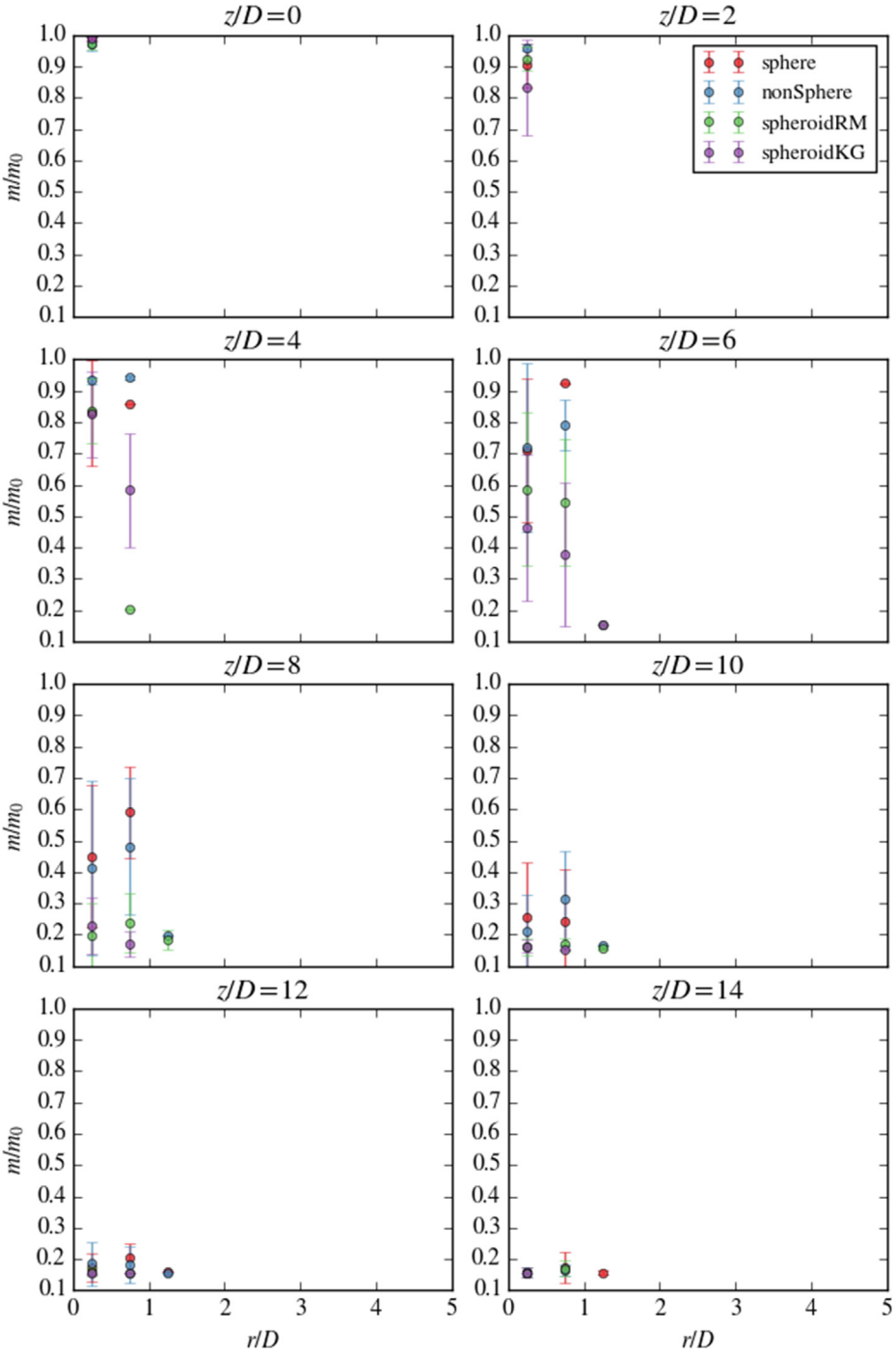

Fig. 10. Normalized particle mass along reactor radius (r/D) at different height (z/D) along the reactor. Round dots with error bars are average normalized masses for particles and their standard deviations.

followed the main flow of the surrounding gas and travelled further downstream, where they were heated up and started drying and devolatilization processes, making their normalized mass decreased. Around the axial location of $z/D = 14$, normalized particle masses in all cases are close to 0.15, meaning that particles finished most or all of the drying and devolatilization processes. This is in line with the fact that all biomass particles were configured with 15.4% wt (weight) of char and ash.

Even though the final output is similar in all four cases, differences in their histories are still present. Their differences are insignificant in the beginning, because drying and devolatilization just began. As z/D increases, their differences start to manifest and become obvious at reactor axial location of $z/D = 6$. Normalized particle masses decrease faster in *Case 3* (spheroidRM) and *Case 4* (spheroidKG) than in *Case 1* (sphere) and *Case 2* (nonSphere). Such differences are most pronounced at reactor axial location of $z/D = 6$. This is believed to be caused by their different particle surface areas. *Case 3* (spheroidRM) and *Case 4* (spheroidKG) are based on the assumption of particles being spheroids, and their surface areas were accordingly adjusted, whereas *Case 1* (sphere) and *Case 2* (nonSphere) essentially simulated particles as spheres of equivalent volume. As a result, the particle surface areas are larger in *Case 3* (spheroidRM) and *Case 4* (spheroidKG) when compared with the ones in *Case 1* (sphere) and *Case 2* (nonSphere), and thus subject to better heat transfer. The difference between *Case 1* (sphere) and *Case 2* (nonSphere) is due to the hydrodynamic models applied, as it is the only difference between the initial configurations of these two cases. The difference between *Case 3* (spheroidRM) and *Case 4* (spheroidKG) is due to the heat transfer models applied, as evidenced in Fig. 11, which shows the Nusselt number ratio predicted by the two heat transfer models at different Prandtl and Reynolds number with ranges that are applicable in an entrained flow gasifier (see discussion in Section 2.2). One can see that the Kishore-Gu model favors heat transfer more than the Ranz-Marshall model under current operating conditions. However, all the differences among these four cases become smaller again when z/D increases from 10 to 14. At this stage, the majority of the particles have finished most or all of their drying and devolatilization processes, their masses and surface areas became much smaller, and differences in hydrodynamic and heat transfer models are less relevant.

4.2.2. Axial velocities of gas flow and particles

In the previous section, only particles with short residence time are sampled to filter out particles that are in recirculation. This is useful when drying and devolatilization processes are of interest. However, to capture a more realistic representation of the reactor, flow axial velocities of flow fields of all particles along reactor radius (r/D) at different height (z/D) of the reactor are shown in Fig. 12. Gas flow axial velocities of the four cases are similar with minor differences, so the flow axial velocity of *Case 1* (sphere) is used to represent the flow fields and it is marked by an orange dashed line. In the beginning where the axial location is $z/D = 0$, the flow axial velocity is represented by a plateau within $r/D \leq 0.5$, where the biomass particles were injected via inner central tube. The gas flow axial velocity reaches a maximum where the secondary air was injected, then decreases again as r/D increases. This is due to that primary and secondary air flows were injected at different rates. As z/D increases, gas flows at different radial positions mix, but they still have relatively high axial velocities due to thermal expansion. One can also observe that axial velocities of the gas flows and particles are negative in regions where r/D is relatively large. This means that there are recirculation zones in the gas flow fields. Further downstream, gas temperatures are expected to drop and axial velocities of gas flow decrease.

Particles' axial velocities of the four cases are marked with dots with error bar. It can be seen that they generally follow the flow field, especially near the inlet and far away from the inlet. In the intermediate axial locations of z/D = 5–20, particle axial velocity differs among these four cases. With exceptions, one can conclude that particles with spheroidal shapes have higher axial velocities. However, it is difficult to determine the extent of each factor's influence as the situation is complex with many changing variables. In these axial locations, rapid devolatilization occurs, particles in different cases are subject to different velocity and temperature fields, different particle hydrodynamic and heat transfer models and different mass loses; all of which could make particle axial velocity differences more pronounced in this intermediate axial region among these four cases. Further downstream at axial locations of $z/D \geq 35$, drying and devolatilization are presumably complete, biomass particles lose majority of their mass, thus reducing inertia and making them follow more closely the flow fields as observed in Fig. 12.

4.2.3. Particle orientation

Particle alignment angle, previously defined as the angle between the particle major axis and the gravity direction, is a good representation of particle orientation. In a similar manner, Fig. 13 shows probability density distribution of particle alignment angles of *Case 3* (spheroidRM) and *Case 4* (spheroidKG) at different height (z/D) of the reactor. Both have similar trends and do not exhibit significant differences. At axial location of $z/D = 0$, a small portion of particles have alignment angles close to 0° while the rest close to 90°, this agrees with the initial configurations of particle orientations where each 1/3 of particle were injected with major axis parallel to *x*-, *y*- and *z*-direction, respectively. Then when z/D increases from 5 to 20, particle alignment angles tend to move more to 0°. However, this trend does not hold further downstream. When z/D increases to 50, no preferential pattern of particle alignment angles can be seen, and particles are randomly oriented. As previously stated, it is probably due to velocity gradients, which can be observed from Fig. 12, especially when z/D ranges from 5 to 20, making particles more preferably aligned to 0° (flow direction). At axial location of $z/D = 50$, no significant axial velocity gradients can be seen in Fig. 12, making particle alignment isotropic. This argument is further supported by Fig. 14, where alignment angles for particles at axial position of $z/D = 5$ are sampled and plotted separately, depending on whether the sampled particle is within or outside the radial location of $r/D = 2$. Particles at radial positions $r/D \leq 2$ tend to have alignment angles closer to 0° (see Fig. 14) and the gas flow at the radial position of $r/D \leq 2$ exhibits large gradients in axial velocities (see Fig. 12), compared to what is observed for $r/D > 2$. One can therefore conclude that particle orientations are dependent on gas flow velocity gradient.

4.2.4. Syngas production and particle residence time

As demonstrated above, the spheroidal particle approach affects the histories of the particle through the reactor domain. In order to investigate the effect on the final gas composition at outlet, mass fractions

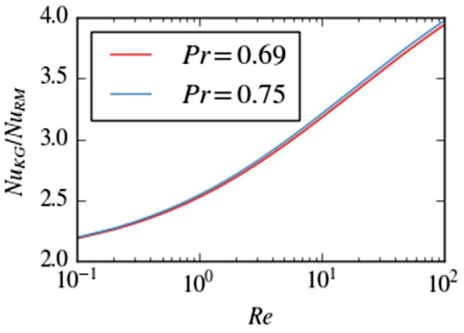

Fig. 11. Nusselt number, *Nu*, ratio predicted by two heat transfer models at different Prandtl number, *Pr*, and Reynolds number, *Re*. Subscript *KG* and *RM* represent the Kishore-Gu and Ranz-Marshall model, respectively. Particle aspect ratio is 10. The validity for the ranges of *Pr* and *Re* is discussed in Section 2.2.

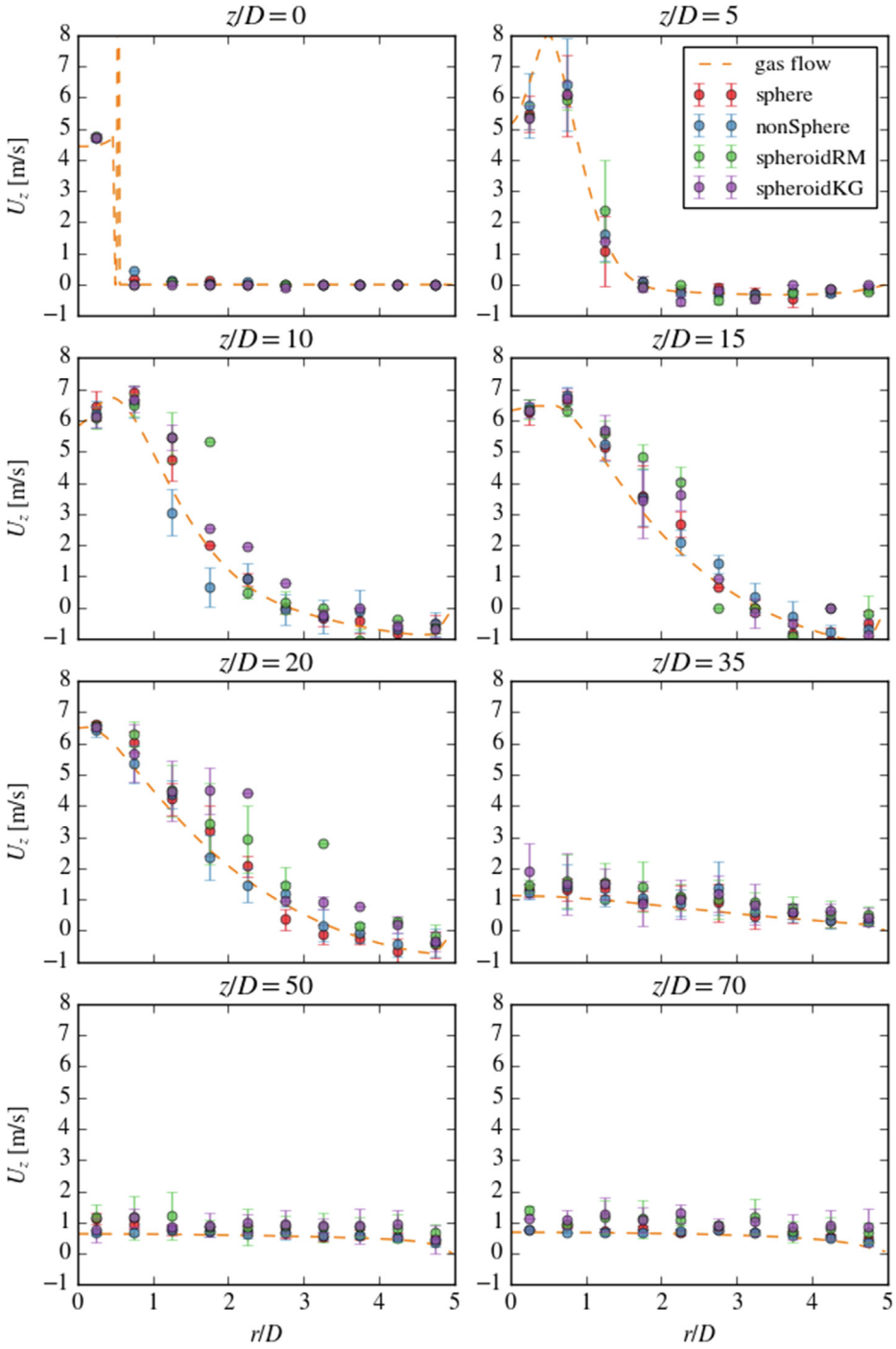

Fig. 12. Axial velocities of gas flow and all particles along reactor radius (r/D) at different height (z/D) along the reactor. Different color represents difference cases as shown in the legend. Round dots with error bars are particle average velocities and their standard deviations. Dash lines are flow field velocities.

of CO are shown in Fig. 15 to indicate syngas productions in the entrained flow reactor. At axial location of z/D = 0–15 where devolatilization are expected to be dominant, especially in the central radial region, mass fractions of syngas increase rapidly. As z/D increases further, char conversion, which is comparably slower, plays a more important role, and mass fractions of CO increase much slower and more evenly along the radial direction. When comparing the four cases, one can see that their differences are most pronounced at axial location of z/D = 5. *Case 4* (spheroidKG) has the highest mass fractions of syngas, *Case 3* (spheroidRM) comes second, while *Case 1* (sphere) and *Case 2* (nonSphere) come last. This agrees with what is observed in Fig. 10 regarding particle masses. Around the similar axial location, *Case 4* (spheroidKG) has the highest mass loses, thus release more CO. The mass fractions of *Case 1* (sphere) and *Case 2* (nonSphere) catch up later at axial location of z/D = 10–20, due to the delay of particle thermochemical conversions. Around these axial locations, particles in *Case 1* (sphere) and *Case 2* (nonSphere) are still in the middle of devolatilization, whereas particles in *Case 3* (spheroidRM) and *Case 4* (spheroidKG) are comparably more subject to the slower char conversions. As z/D increases further, mass fractions of CO are almost the same for all the cases. One can postulate that most particles enter char conversion processes there, their particle masses and surface areas are much less when compared to their initial values, hence the differences in particle hydrodynamic models and heat transfer models are much

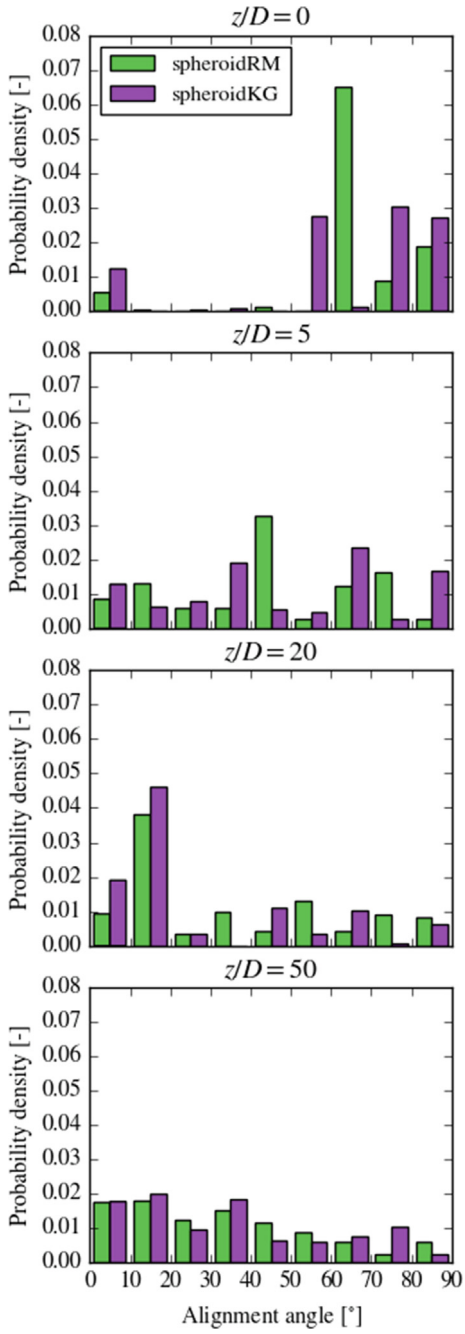

Fig. 13. Probability density of particle alignment angle at different height (z/D) of the reactor.

less relevant. In addition, it seems that particle residence time plays a more important role. In Fig. 16, particle ages along reactor radial direction at reactor outlet (z/D = 70) are plotted. Particle age is defined as the time taken from injection to measurement and can therefore be used to represent particle residence time. It can be seen that particles with spheroidal shape assumptions have shorter residence times than the others. This corresponds to the observation of Fig. 12 that particles with spheroidal shape assumptions have higher axial velocities at axial location of z/D = 5–20. Based on post-processing calculations, the average residence times of particles sampled in Fig. 16 for *Case 1–4* are 4.5 s, 4.0 s, 2.8 s and 2.8 s, respectively. Residence times of *Case 3* (spheroidRM) and *Case 4* (spheroidKG) are almost the same. This means that particle residence time is insensitive to the choice of heat transfer model. Since particle residence time is connected to particle motion, such results also indicate that the choice of heat transfer model does not alter particle hydrodynamics significantly. However, the residence times of *Case 1* (sphere) and *Case 2* (nonSphere) are 61% and 43% longer than *Case 4* (spheriodKG), respectively. This is due to the different hydrodynamic models employed. It should be noted that residence time plays an important role in chemical reactions. Even though particles in cases of spheroidal shape assumptions have more surface area for mass and heat transfer, *Case 1* (sphere) and *Case 2* (nonSphere) have longer particle residence times for particles to react, which is very relevant for slow process like char conversion.

However, it would be wrong to conclude that the choices of models of particle shape, hydrodynamics and heat transfer are not important. Particularly, if localized information of particles inside the reactor is more of interest, for example, for optimizing gasifier operation based on localized information (such as sintering at the walls), different model selections yield to different results, as stated above. But it seems that the tested particle models do not affect the syngas production rate at the outlet under current operating conditions. This most likely is due to the simplification applied in the study. For example, an isothermal boundary condition was configured in the simulations, based on the average value from only a few measurement points in the experiments. However, gasifiers in reality are expected to be operated in autothermal mode, thus the temperature of the gasifier wall is directly influenced by the particle conversion, instead of remaining constant in the current simulations. Moreover, current simulations use simplified chemical kinetic models, which might be insensitive to the differences of current four model configurations. Therefore, it is reasonable to believe differences in syngas production can be anticipated in future work if these potential issues could be properly addressed.

5. Conclusions

In this work, a new spheroid model for particle hydrodynamics, a heat transfer model for spheroids and a new set of parameters for devolatilization kinetics have been implemented in OpenFOAM. Simulations and experiments of a laminar flow drop tube reactor have

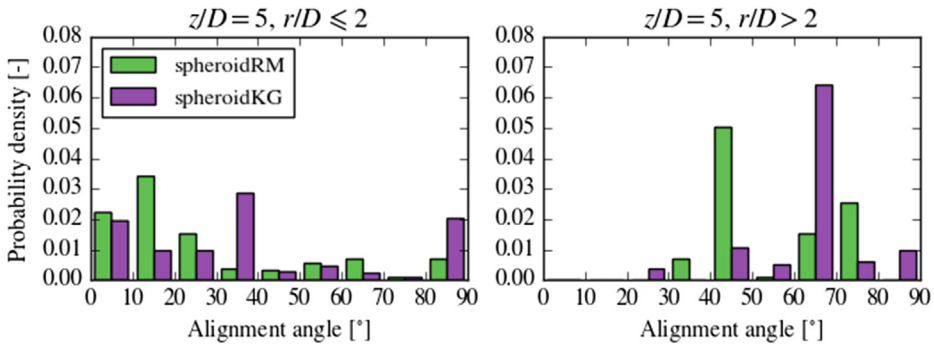

Fig. 14. Probability density of particle alignment angle at axial location of z/D = 5; (a) only include particles at the radial position of $r/D \leq 2$; (b) only include particles at the radial position of $r/D > 2$.

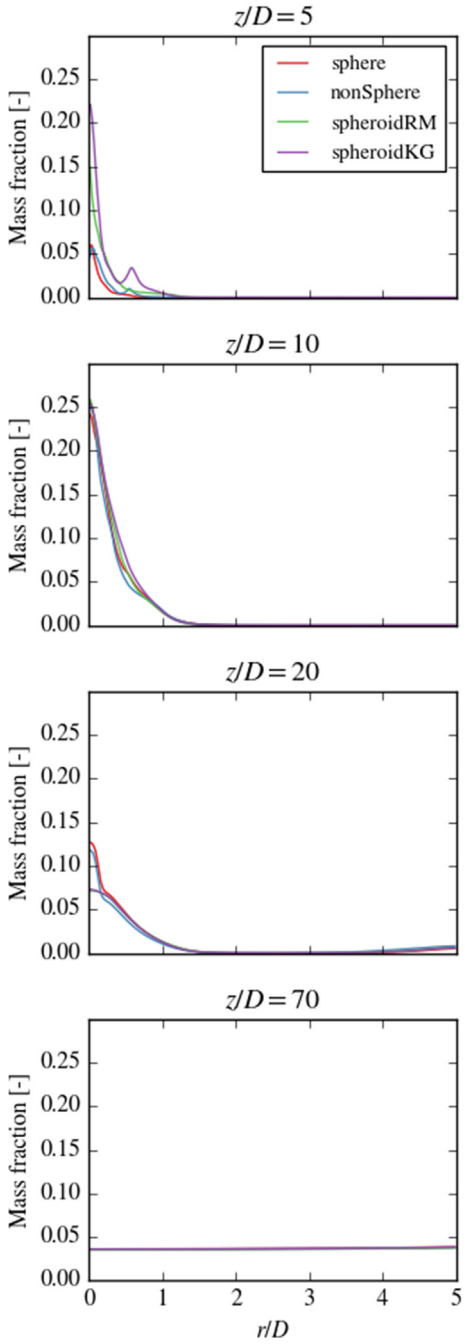

Fig. 15. Mass fractions of CO along reactor radius (r/D) at different height of reactor (z/D).

been conducted. Based on the comparisons between experiments and simulations, the three new models have been further validated under reactive conditions. In addition, simulations with configurations similar to an entrained flow gasifier have been executed. Four different approaches involving different particle shapes, hydrodynamics and heat transfer models have been employed for quantitative comparison analyses. The spheroidal particle shape assumption with adjusted spheroidal surface area and the Kishore-Gu model proves to favor particle thermochemical conversions, especially during drying and devolatilization process. However, the sphere and simplified non-sphere model predict 61% and 43% longer residence times, respectively, than the spheroid models, and longer residence time seems to favor the char conversion process. These factors have opposite effects on the total thermal conversion of the biomass particles and seem to compensate

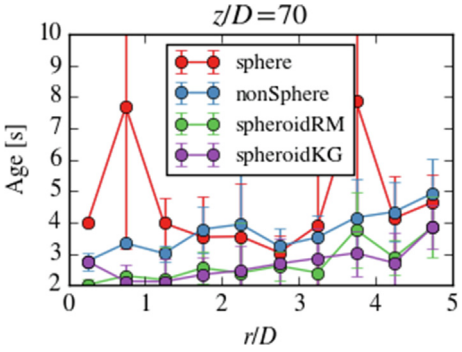

Fig. 16. Particle age along reactor radius at $z/D = 70$ (outlet). Round dots with error bars are particle average ages and their standard deviations.

each other, making the overall syngas production at the outlet less affected by the choice of models, even though their differences are clearly seen in otherwise located regions. This could be caused by the isothermal temperature configuration at the walls and simplified chemical kinetics employed in the simulations. Particle orientation's dependency on velocity gradients even under reactive conditions are repeatedly found, agreeing with other researchers' work under non-reactive conditions.

CRediT authorship contribution statement

Ning Guo: Conceptualization, Methodology, Software, Validation, Formal analysis, Investigation, Data curation, Writing - original draft, Writing - review & editing, Visualization, Project administration. **Ángel David García Llamas:** Software, Validation, Investigation, Data curation, Writing - review & editing, Visualization, Project administration. **Tian Li:** Software, Validation, Formal analysis, Data curation, Writing - review & editing, Supervision. **Kentaro Umeki:** Resources, Writing - review & editing, Supervision, Funding acquisition. **Rikard Gebart:** Writing - review & editing, Supervision. **Terese Løvås:** Resources, Writing - review & editing, Supervision, Funding acquisition.

Acknowledgement

The authors would like to acknowledge Research Council of Norway and industrial partners to fund this work via GAFT project (No. 244069). Moreover, the authors greatly appreciate Norrbotten Research Council and Kempe Foundation in Sweden for supporting the experimental campaign carried in this work. We also extend our gratitude to Dr. Kathrin Weber for useful discussions of biomass properties. Furthermore, UNINET Sigma2 and NTNU HPC Group provided high-performance computational resources for CFD simulations.

Appendix A. Supplementary data

Supplementary data to this article can be found online at https://doi.org/10.1016/j.fuel.2020.117495.

References

[1] IEA. CO2 Emissions from Fuel Combustion 2018. Paris: OECD; 2018. DOI: 10.1787/co2_fuel-2018-en.
[2] Liaquat AM, Kalam MA, Masjuki HH, Jayed MH. Potential emissions reduction in road transport sector using biofuel in developing countries. Atmos Environ 2010. https://doi.org/10.1016/j.atmosenv.2010.07.003.
[3] Zwart RWR, Boerrigter H, van der Drift A. The impact of biomass pretreatment on the feasibility of overseas biomass conversion to Fischer-Tropsch products. Energy Fuels 2006;20:2192–7. https://doi.org/10.1021/ef060089f.
[4] Sikarwar VS, Zhao M, Clough P, Yao J, Zhong X, Memon MZ, et al. An overview of advances in biomass gasification. Energy Environ Sci 2016;9:2939–77. https://doi.org/10.1039/C6EE00935B.
[5] Li T, Wang L, Ku X, Güell BM, Løvås T, Shaddix CR. Experimental and modeling

study of the effect of torrefaction on the rapid devolatilization of biomass. Energy Fuels 2015;29:4328–38. https://doi.org/10.1021/acs.energyfuels.5b00348.
[6] Gubba SR, Ma L, Pourkashanian M, Williams A. Influence of particle shape and internal thermal gradients of biomass particles on pulverised coal/biomass co-fired flames. Fuel Process Technol 2011;92:2185–95. https://doi.org/10.1016/j.fuproc.2011.07.003.
[7] Panahi A, Levendis YA, Vorobiev N, Schiemann M. Direct observations on the combustion characteristics of Miscanthus and Beechwood biomass including fusion and spherodization. Fuel Process Technol 2017;166:41–9. https://doi.org/10.1016/j.fuproc.2017.05.029.
[8] Gao X, Zhang Y, Li B, Yu X. Model development for biomass gasification in an entrained flow gasifier using intrinsic reaction rate submodel. Energy Convers Manage 2016;108:120–31. https://doi.org/10.1016/j.enconman.2015.10.070.
[9] Ku X, Jin H, Lin J. Comparison of gasification performances between raw and torrefied biomasses in an air-blown fluidized-bed gasifier. Chem Eng Sci 2017;168:235–49. https://doi.org/10.1016/j.ces.2017.04.050.
[10] Simone M, Biagini E, Galletti C, Tognotti L. Evaluation of global biomass devolatilization kinetics in a drop tube reactor with CFD aided experiments. Fuel 2009;88:1818–27. https://doi.org/10.1016/j.fuel.2009.04.032.
[11] Zhang W, Watanabe H, Kitagawa T. Direct numerical simulation of ignition of a single particle freely moving in a uniform flow. Adv Powder Technol 2017;28:2893–902. https://doi.org/10.1016/j.apt.2017.08.016.
[12] Zhang W, Tainaka K, Ahn S, Watanabe H, Kitagawa T. Experimental and numerical investigation of effects of particle shape and size distribution on particles' dispersion in a coaxial jet flow. Adv Powder Technol 2018. https://doi.org/10.1016/j.apt.2018.06.008.
[13] Zhang W, Watanabe H, Kitagawa T. Numerical investigation of effects of particle shape on dispersion in an isotropic turbulent flow. Adv Powder Technol 2018;29:2048–60. https://doi.org/10.1016/j.apt.2018.05.011.
[14] Riaza J, Gibbins J, Chalmers H. Ignition and combustion of single particles of coal and biomass. Fuel 2017;202:650–5. https://doi.org/10.1016/J.FUEL.2017.04.011.
[15] Lu H, Ip E, Scott J, Foster P, Vickers M, Baxter LL. Effects of particle shape and size on devolatilization of biomass particle. Fuel 2010;89:1156–68. https://doi.org/10.1016/J.FUEL.2008.10.023.
[16] Trubetskaya A, Beckmann G, Wadenbäck J, Holm JK, Velaga SP, Weber R. One way of representing the size and shape of biomass particles in combustion modeling. Fuel 2017;206:675–83. https://doi.org/10.1016/J.FUEL.2017.06.052.
[17] Haider A, Levenspiel O. Drag coefficient and terminal velocity of spherical and nonspherical particles. Powder Technol 1989;58:63–70. https://doi.org/10.1016/0032-5910(89)80008-7.
[18] Zastawny M, Mallouppas G, Zhao F, van Wachem B. Derivation of drag and lift force and torque coefficients for non-spherical particles in flows. Int J Multiph Flow 2012;39:227–39. https://doi.org/10.1016/j.ijmultiphaseflow.2011.09.004.
[19] Rosendahl L. Using a multi-parameter particle shape description to predict the motion of non-spherical particle shapes in swirling flow. Appl Math Model 2000;24:11–25. https://doi.org/10.1016/S0307-904X(99)00023-2.
[20] Hölzer A, Sommerfeld M. New simple correlation formula for the drag coefficient of non-spherical particles. Powder Technol 2008;184:361–5. https://doi.org/10.1016/j.powtec.2007.08.021.
[21] Jeffery GB. The motion of ellipsoidal particles immersed in a viscous fluid. Proc R Soc A Math Phys Eng Sci 1922;102:161–79. https://doi.org/10.1098/rspa.1922.0078.
[22] Guo N, Li T, Zhao L, Løvås T. Eulerian-Lagrangian simulation of pulverized biomass jet using spheroidal particle approximation. Fuel 2019;239:636–51. https://doi.org/10.1016/j.fuel.2018.10.137.
[23] Li J, Zhang J. Analytical study on char combustion of spheroidal particles under forced convection. Powder Technol 2017;313:210–7. https://doi.org/10.1016/j.powtec.2017.02.054.
[24] Tabet F, Gökalp I. Review on CFD based models for co-firing coal and biomass. Renew Sustain Energy Rev 2015;51:1101–14. https://doi.org/10.1016/J.RSER.2015.07.045.
[25] Bhuiyan AA, Naser J. Computational modelling of co-firing of biomass with coal under oxy-fuel condition in a small scale furnace. Fuel 2015;143:455–66. https://doi.org/10.1016/J.FUEL.2014.11.089.
[26] Bonefacic I, Frankovic B, Kazagic A. Cylindrical particle modelling in pulverized coal and biomass co-firing process. Appl Therm Eng 2015;78:74–81. https://doi.org/10.1016/j.applthermaleng.2014.12.047.
[27] Yin C, Rosendahl L, Kær S SK, Condra TJ. Use of numerical modeling in design for co-firing biomass in wall-fired burners. Chem Eng Sci 2004;59:3281–92. https://doi.org/10.1016/J.CES.2004.04.036.
[28] Ku X, Li T, Løvås T. Eulerian-Lagrangian simulation of biomass gasification behavior in a high-temperature entrained-flow reactor. Energy Fuels 2014;28:5184–96. https://doi.org/10.1021/ef5010557.
[29] Ku X, Li T, Løvås T. Effects of particle shrinkage and devolatilization models on high-temperature biomass pyrolysis and gasification. Energy Fuels 2015;29:5127–35. https://doi.org/10.1021/acs.energyfuels.5b00953.
[30] Ku X, Li T, Løvås T. CFD-DEM simulation of biomass gasification with steam in a fluidized bed reactor. Chem Eng Sci 2015;122:270–83. https://doi.org/10.1016/j.ces.2014.08.045.
[31] Johansen JM, Jensen PA, Glarborg P, De Martini N, Ek P, Mitchell RE. High heating rate devolatilization kinetics of pulverized biomass fuels. Energy Fuels 2018;32:12955–61. https://doi.org/10.1021/acs.energyfuels.8b03100.
[32] Ranz WE, Marshall Jr. WR. Evaporation from drops - part I. Chem Eng Prog 1952.
[33] Ranz WE, Marshall Jr. WR. Evaporation from drops - part II. Chem Eng Prog 1952.
[34] Kishore N, Gu S. Effect of blockage on heat transfer phenomena of spheroid particles at moderate Reynolds and Prandtl numbers. Chem Eng Technol 2011;34:1551–8. https://doi.org/10.1002/ceat.201100007.
[35] Kriebitzsch S, Richter A. LES simulation of char particle gasification at Reynolds numbers up to 1000. Combust Flame 2020;211:185–94. https://doi.org/10.1016/J.COMBUSTFLAME.2019.08.028.
[36] Johansen JM, Gadsbøll R, Thomsen J, Jensen PA, Glarborg P, Ek P, et al. Devolatilization kinetics of woody biomass at short residence times and high heating rates and peak temperatures. Appl Energy 2016;162:245–56. https://doi.org/10.1016/j.apenergy.2015.09.091.
[37] Li T, Niu Y, Wang L, Shaddix C, Løvås T. High temperature gasification of high heating-rate chars using a flat-flame reactor. Appl Energy 2018;227:100–7. https://doi.org/10.1016/j.apenergy.2017.08.075.
[38] Tolvanen H, Keipi T, Raiko R. A study on raw, torrefied, and steam-exploded wood: fine grinding, drop-tube reactor combustion tests in N2/O2 and CO2/O2 atmospheres, particle geometry analysis, and numerical kinetics modeling. Fuel 2016;176:153–64. https://doi.org/10.1016/j.fuel.2016.02.071.
[39] Elfasakhany A, Tao L, Espenas B, Larfeldt J, Bai XS. Pulverised wood combustion in a vertical furnace: experimental and computational analyses. Appl Energy 2013;112:454–64. https://doi.org/10.1016/j.apenergy.2013.04.051.
[40] Njobuenwu DO, Fairweather M. Simulation of inertial fibre orientation in turbulent flow. Phys Fluids 2016;28:063307https://doi.org/10.1063/1.4954214.
[41] Simonsson J, Bladh H, Gullberg M, Pettersson E, Sepman A, Ögren Y, et al. Soot concentrations in an atmospheric entrained flow gasifier with variations in fuel and burner configuration studied using diode-laser extinction measurements. Energy Fuels 2016;30:2174–86. https://doi.org/10.1021/acs.energyfuels.5b02561.
[42] Thunman H, Niklasson F, Johnsson F, Leckner B. Composition of volatile gases and thermochemical properties of wood for modeling of fixed or fluidized beds. Energy Fuels 2001;15:1488–97. https://doi.org/10.1021/ef010097q.
[43] Haseli Y, van Oijen JA, de Goey LPH. A detailed one-dimensional model of combustion of a woody biomass particle. Bioresour Technol 2011;102:9772–82. https://doi.org/10.1016/j.biortech.2011.07.075.